Joule

Article

Complex formation of ferrocene derivatives with electron transport layers enables improved performance and photostability in organic solar cells

Graphical abstract

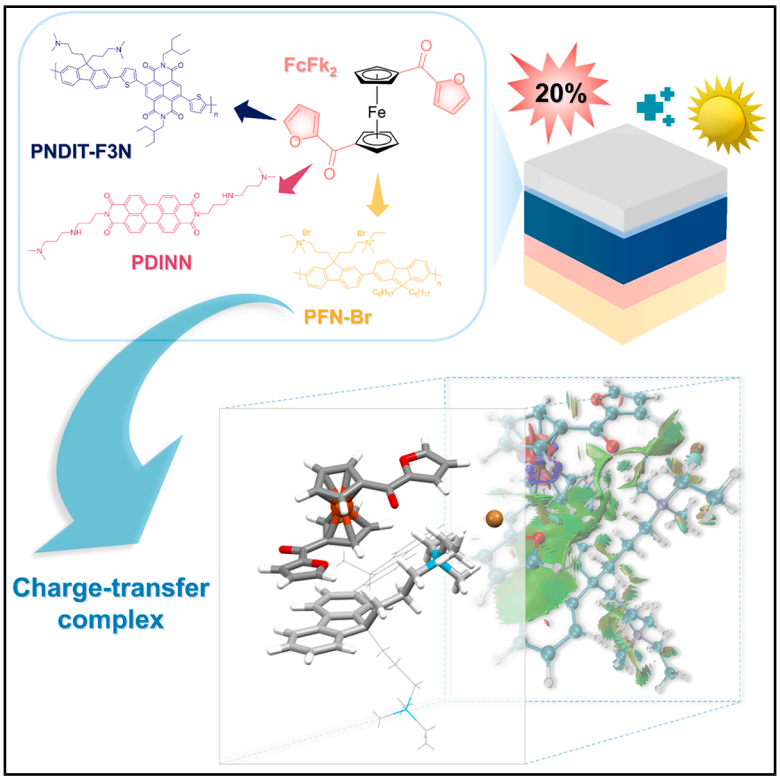

Highlights

- Complex formation between ferrocene derivatives and ETLs leads to FF > 80%
- Ternary blends using the hybrid organic-inorganic ETLs achieve a PCE of 20.1%
- We demonstrated the universality of hybrid ETLs in 8 different OSC systems
- Enhanced photostability, with 700 h T_{80} under operating condition degradation

Authors

Patipan Sukpoonprom, William D. J. Tremlett, Zhuoran Qiao, ..., Derya Baran, Nicholas J. Long, Nicola Gasparini

Correspondence

n.long@imperial.ac.uk (N.J.L.), n.gasparini@imperial.ac.uk (N.G.)

In brief

This study presents the complex formation between ferrocene derivatives and n-type materials used as electron-transporting layers (ETLs) in OSCs. By fine-tuning the work function of these novel hybrid ETLs, OSC devices delivered enhanced charge extraction with fill factor exceeding 80% and consequently power conversion efficiency > 20%. Due to reduced trap-assisted recombination in the hybrid ETL devices, we demonstrated improved photostability with 80% of their initial performance retained for over 700 h when degraded under operating condition (ISOS-L-1I).

Sukpoonprom et al., 2025, Joule 9, 102107
October 15, 2025
https://doi.org/10.1016/j.joule.2025.102107

CellPress

Joule

CellPress
OPEN ACCESS

Article

Complex formation of ferrocene derivatives with electron transport layers enables improved performance and photostability in organic solar cells

Patipan Sukpoonprom,[1,2,7] William D.J. Tremlett,[1,7] Zhuoran Qiao,[1,7] Chitsanucha Chattakoonpaisarn,[2] Eunyoung Hong,[1] Beier Hu,[1] Karen Forberich,[3] Jianhua Han,[4] Junyi Wang,[1] Somlak Ittisanronnachai,[5] Longren Li,[1] Francesco Vanin,[6] Pichaya Pattanasattayavong,[2] Zonglong Zhu,[6] Artem Bakulin,[1] Christoph J. Brabec,[3] Derya Baran,[4] Nicholas J. Long,[1,*] and Nicola Gasparini[1,8,*]

[1]Department of Chemistry and Centre for Processable Electronics, Imperial College London, London W12 0BZ, UK
[2]Department of Materials Science and Engineering, School of Molecular Science and Engineering, Vidyasirimedhi Institute of Science and Technology (VISTEC), Rayong 21210, Thailand
[3]Institute of Materials for Electronics and Energy Technology (I-MEET), Friedrich-Alexander-University Erlangen-Nuremberg, Erlangen 91058, Germany
[4]Materials Science and Engineering Program (MSE), Physical Sciences and Engineering Division (PSE), King Abdullah University of Science and Technology (KAUST), Thuwal 23955-6900, Saudi Arabia
[5]Frontier Research Center (FRC), Vidyasirimedhi Institute of Science and Technology (VISTEC), Rayong 21210, Thailand
[6]Department of Chemistry and Hong Kong Institute of Clean Energy, City University of Hong Kong, Kowloon 999077, Hong Kong, China
[7]These authors contributed equally
[8]Lead contact
*Correspondence: n.long@imperial.ac.uk (N.J.L.), n.gasparini@imperial.ac.uk (N.G.)
https://doi.org/10.1016/j.joule.2025.102107

CONTEXT & SCALE Organic solar cells (OSCs) are promising and environmentally benign sources of energy, with power conversion efficiency now exceeding 20%. The high performance in OSCs is mainly achieved by the optimization of the photoactive layer, with less focus on developments of electron-transporting layers (ETLs). Herein, we report the formation of a charge-transfer complex between newly synthesized ferrocene (Fc) derivatives and ETLs to facilitate electron extraction. Computational simulation, elemental, and opto-electronic characterizations reveal the chemical interactions and work function tuning of hybrid ETLs. With the rational design of Fc derivatives, we showed improved performances in various OSC systems with different ETLs, with the highest efficiency of 20.1% and enhanced photostability with T_{80} of 700 h under operating conditions.

SUMMARY

Electron transport layers (ETLs), e.g., metal oxides, organic small molecules, or conjugated polymers, play a vital role in both performance and photo-thermal stability in organic solar cells (OSCs). Herein, we explored hybrid organic-inorganic electron transport materials by forming complexes between typical electron transport layers and ferrocene (Fc)-based molecules. Experimental and theoretical investigations revealed van der Waals interaction between the ETL and Fc compounds, which allows fine-tuning of the electrode work function to improve charge extraction properties and reduce trap-assisted recombination. As a result, OSCs showed improved fill factor (FF) and power conversion efficiency (PCE) for five donor-acceptor blends and three ETLs, with FF and PCE exceeding 80% and 20.1%, respectively. Finally, we demonstrated improved photostability for the hybrid ETLs with devices that retained 80% of their initial performance for 700 h when degraded under operating conditions (ISOS-L-1I).

INTRODUCTION

Organic solar cells (OSCs) are gaining tremendous attention as promising green energy technologies owing to their abundant non-toxic carbon-based nature, processability in ambient environments using benign solvents, and ability to allow devices and modules to be compatible with conformable surfaces.[1–3] The power conversion efficiency (PCE) of OSCs has been propelled by designing and developing photoactive materials, i.e., polymer donors and non-fullerene

acceptors (NFAs), to exceed 20% in binary and ternary systems.[4,5] Moreover, the development of the hole transport layers (HTLs) and electron transport layers (ETLs) plays a vital role to achieve efficient and photo-stable OSCs simultaneously.[6] Tuning the work function of electrodes to establish better Ohmic contacts and hence improve charge carrier selectivity and device stability is one of the most common strategies.[7–9] For conventional architectures, in addition to the common materials, such as poly(2,3-dihydrothieno-1,4-dioxin)-poly(styrenesulfonate) (PEDOT:PSS) and copper(I) thiocyanate (CuSCN),[10,11] research efforts have been directed toward the class of self-assembled monolayer (SAM) materials, e.g., 2PACz, in both OSCs and perovskite devices due to their tunable energetics and surface energy.[12,13] Differently, very few choices are available for ETLs, where water/alcohol-soluble conjugated polyelectrolytes, poly(9,9-bis(3'-(N,N-dimethyl)-N-ethylammoinium-propyl-2,7-fluorene)-alt-2,7-(9,9-dioctyl-fluorene))dibromide (PFN-Br) or poly[[2,7-bis(2-ethylhexyl)-1,2,3,6,7,8-hexahydro-1,3,6,8-tetraoxobenzo[lmn] [3,8]phenanthroline-4,9-diyl]-2,5-thiophenediyl[9,9-bis[3'((N,N-dimethyl)-N-ethylamino) propyl]-9H-fluorene-2,7-diyl]-2,5-thiophenediyl] (PNDIT-F3N), are the common choices.[14,15] For example, the PFN^+ and Br^- moieties can create a dipole moment pointing to the silver (Ag) electrode. Therefore, the induced high electron density at the Ag interface leads to a reduced work function, which can facilitate electron collection efficiency.[16] However, the polyfluorene backbone of PFN-Br intrinsically demonstrates an electron-rich unit, which is detrimental to electron transport properties.

Hybrid organic-inorganic electron transport materials have been explored in recent years due to the superior electron mobility and conductivity of formed charge-transfer (CT) complexes.[17,18] Ferrocene (Fc) and its derivatives have emerged as potential candidates for ETLs owing to the strong electron delocalization in the Fc units, which enhances the fill factor (FF) and consequentially the PCE in organic and perovskite solar cells, as well as perovskite photodetectors.[19–22] Ferrocenyl-bis-thiophene-2-carboxylate ($FcTc_2$) has been exploited to passivate interfacial defects of perovskite and improve charge transport due to uniform surface potential distribution.[23] Moreover, perylene diimide (PDIN)-based small molecules have been functionalized with Fc terminating groups, with the hybrid electron extracting layer exhibiting lower Ag work function and improvements in Ohmic contact and charge selectivity.[24] However, these aforementioned ETLs require several synthetic steps alongside batch-to-batch variation and considerable material cost. Hence, low-cost, scalable, and versatile properties of ETL materials are still urgently needed to achieve significant development in performance and stability.

In this work, we report a simple multicomponent route to fine-tune the ETL/Ag work function to facilitate electron extraction from the bulk heterojunction (BHJ). We found that adding the Fc derivative, ferrocenyl-bis-furyl-2-ketone ($FcFk_2$), into common ETLs (PFN-Br, PDINN, and PNDIT-F3N) led to improved FF and PCE, with values exceeding 80% and 20.1%, respectively. Our theoretical and experimental investigations demonstrated a CT complex formation between $FcFk_2$ and the ETLs, which reduces trap-assisted recombination at the BHJ and ETL interface. In addition, this robust ETL complex, PFN-Br:$FcFk_2$, allowed OSCs to achieve superior photostability (retaining 80% of an initial PCE over 700 h) under the ISOS-L-1I degradation protocol.

RESULTS AND DISCUSSION

Selection of Fc-based molecules

Fc and two derivatives, decamethylferrocene ($Me_{10}Fc$) with electron-donating groups and $FcFk_2$ with electron-withdrawing groups, were used to study the effect of Fc-based compounds within ETLs in OSC devices. Through the simplicity of synthetic and purification steps, we produced $FcFk_2$ in >16% yield utilizing low-cost materials for as little as £8.2 ($10.4 USD) per gram. Synthetic steps, structural identification, and electrochemical characterization are reported in Scheme S1, Figures S1–S6, and Table S1. The Fc-based chemical structures are depicted in Figure 1A, while the absorption spectra of Fc-, $Me_{10}Fc$-, and $FcFk_2$-mixed PFN-Br films, denoted as PFN-Br:Fc, PFN-Br:$FcMe_{10}Fc$, and PFN-Br:$FcFk_2$, respectively, and Tauc plots for optical band gap ($E_{g,opt}$) are shown in Figure S7. The highest occupied molecular orbital (HOMO) levels are obtained by photoemission yield spectroscopy (PYS) in air, depicted in Figure S8, while the lowest unoccupied molecular orbital (LUMO) levels are calculated from the HOMO levels with $E_{g,opt}$, respectively. We calculated HOMO/LUMO level values of −5.35/−2.41 eV for PFN-Br, −5.49/−2.55 eV for PFN-Br:Fc, −5.52/−2.58 eV for PFN-Br:$FcFk_2$, and −5.24/−2.30 eV for PFN-Br:$Me_{10}Fc$. The other relevant photophysical values, e.g., $E_{g,opt}$, are summarized in Figure S9 and Table S2. The deeper HOMO levels, featured by Fc- and $FcFk_2$-hybrid ETLs, can facilitate better hole-blocking capability from the BHJ to Ag electrode to reduce charge recombination.[25,26] For this reason, we investigated the ETL/Ag structures by non-scanning Kelvin probe measurements to determine the work function. Together with the energy levels of PM6 and BTP-eC9, which serve as the donor and acceptor in the BHJ, respectively (see Figure 1B), the measurement helped to reveal the electron selectivity of each system depicted in Figure 1C. PFN-Br effectively modifies the work function of Ag by suppressing it from −4.50 to −4.12 eV, which is a typical property of conjugated polyelectrolytes. Upon the addition of the Fc-based material, Fc and $FcFk_2$ can further lower the work function of Ag to −4.09 and −4.03 eV, respectively, whereas $Me_{10}Fc$ conversely increases the work function to −4.23 eV. When compared with the LUMO of BTP-eC9 (−4.04 eV), the smaller work function difference with ETL/Ag leads to better Ohmic contact, which is beneficial for electron extraction.

To explore the atomic scale of the chemical formation between the Fc derivatives and PFN-Br, we conducted *ab initio* studies by density functional theory (DFT) calculations. For the optimization process,[27] the simulations were set by Gaussian software with the CAM-B3LYP exchange-correlation functional, the basis set of SDD for iron (Fe) atom, and the 6-31++g(d) basis function for all other types of atoms.[28–30] To reduce computational cost and time, the octyl side chains were replaced with

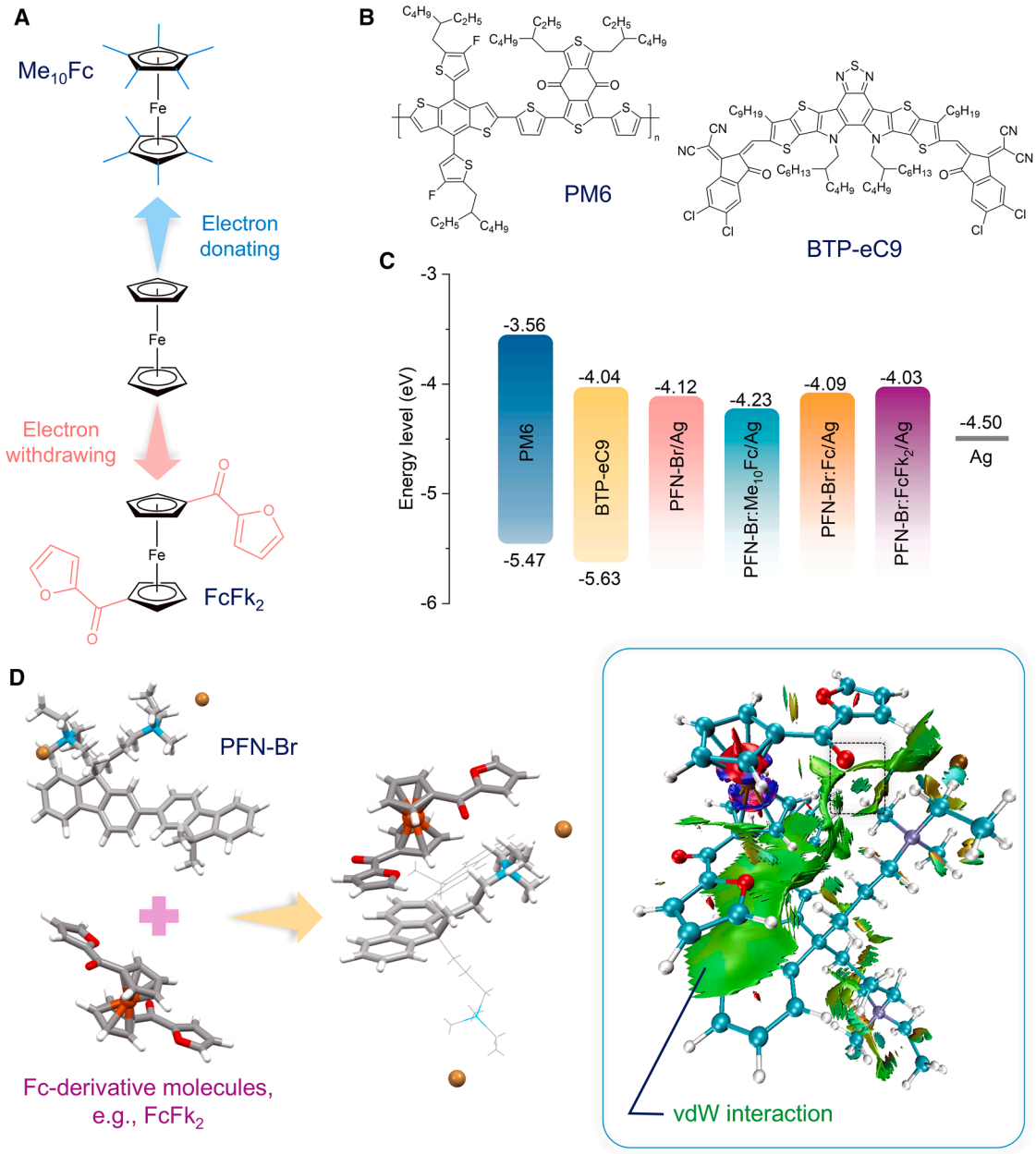

Figure 1. Chemical and photoelectrical profiles

(A) The chemical structures of Fc-based molecules.

(B) The chemical structures of PM6 and BTP-eC9.

(C) The energetics of materials.

(D) Schematic illustrates the mixing between PFN-Br and Fc-derived molecules. The white, gray, red, cyan, brown, and orange sticks or balls are hydrogen (H), carbon (C), oxygen (O), nitrogen (N), bromine (Br), and iron (Fe) atoms, respectively. The optimized molecular structure from DFT calculations for the complex formation between PFN-Br and $FcFk_2$ was demonstrated. This is associated with the coloring map of chemical interactions as shown in the blue border with the inlet-dash-black box, which involves the O atom ($FcFk_2$) and the H atom (ammonium group).

methyl groups. The optimal geometry relaxations were calculated with the Fc molecules positioned either next to the fluorene with the alkyl chains (1st mode) or next to the fluorene with the ammonium groups (2nd mode) of PFN-Br, as displayed in Figures S10–S12.

In Table S3, the optimization energies are summarized for both approaches. The most stable interaction between PFN-Br and Fc showed an optimization energy of −42.6 kJ/mol with Fc positioned over the fluorene moiety with the alkyl chains, whereas the interaction between PFN-Br and $Me_{10}Fc$

displayed an optimization energy of −52.9 kJ/mol with $Me_{10}Fc$ situated over the ammonium groups. The $FcFk_2$ systems exhibited a relaxation energy of −68.4 kJ/mol for the 1st mode, whereas the energy of the 2nd mode (Figure 1D) is dramatically lower at −98.8 kJ/mol, which is the most optimal system among the Fc derivatives studied in this work. Figure S13 showed that the HOMOs (H, H − 1, and H − 2) are predominantly localized on PFN-Br (>99% contribution), while LUMOs (L and L + 1) are mainly located on $FcFk_2$ (>97% contribution). The molecular orbital compositions are shown in Table S4. This distinct separated distribution of frontier orbitals suggests a potential CT pathway from PFN-Br to $FcFk_2$.[31] Therefore, we performed ultraviolet-visible-near infrared (UV-vis-NIR) absorption of PFN-Br, $FcFk_2$, and PFN-Br:$FcFk_2$ (50 mol%; Figures S14A and S14B). We can observe a weak, broad absorption peak from 1,000 to 1,600 nm, which can be attributed to CT absorption.[32] In addition, we carried out photoluminescence (PL) measurements (Figure S14C) showing a red-shifted peak (from 560 to 640 nm, or 0.3 eV) in the NIR region for PFN-Br:$FcFk_2$.[33,34] From the weak intensity of CT absorption band, further investigations are performed in the next section to underpin this point. Interaction region indicator (IRI)[35] in Figure S15 was used to identify the various intermolecular interactions between each compound. Van der Waals (vdW) interactions (green contour in Figure 1D) were found between one of the ammonium groups of the polymer and the carbonyl oxygen (O) in $FcFk_2$, in addition to strong interactions between the fluorene moiety and the furan group on the other cyclopentadienyl (Cp) ring. This suggests the potential interactions between PFN-Br and $FcFk_2$.

Chemical interaction and surface properties of hybrid PFN-Br:$FcFk_2$ ETL

We employed X-ray photoelectron spectroscopy (XPS) to investigate the chemical states of PFN-Br, $FcFk_2$, and PFN-Br:$FcFk_2$. The survey scans displayed in Figure S16 reveal the presence of carbon (C), nitrogen (N), O, Br, and Fe species. In Figures 2A and 2B, the high resolution of O 1*s* and Fe 2*p* core-level spectra of PFN-Br:$FcFk_2$ are compared with pure $FcFk_2$. The core-level profiles of C 1*s*, N 1*s*, and Br 3*d* for all the compounds are shown in Figures S17 and S18. The charge correction acquires binding energy (BE) of C adventitious at 285.0 eV.[36] In Figure 2A, the O 1*s* core-level profile of $FcFk_2$ exhibits two distinct peaks of C=O (carbonyl group) and C–O (furan) at 531.8 and 534.7 eV, respectively.[37–40] The PFN-Br:$FcFk_2$ blend also shows the presence of O bonding from the furan ring at 534.2 eV and the carbonyl group with a slightly higher BE of 532.0 eV. Moreover, we observed an additional O species at 532.7 eV, which is attributed to the BE of O single bonding.[41,42] The new CO–H bonding is formed by O atoms of the carbonyl group in $FcFk_2$ and the H atom of the methyl groups at the ammonium position in PFN-Br, as shown in Figure 1D with the inlet-dash-black box of the color-map interaction.[41,43] The increased oxygen BE of PFN-Br:$FcFk_2$ from 531.8 to 532.0 eV is ascribed to the redistribution of electron density in C=O.

For Fe 2*p* core-level spectra (Figure 2B), $FcFk_2$ respectively shows the doublet peaks of Fe^{2+} $2p_{3/2}$ and $2p_{1/2}$ at BE of 708.7 and 721.3 eV,[44–46] with broad peaks at 711.7 and 725.4 eV assigned to Fe^{2+} satellite peaks.[46–48] Interestingly, the core-level spectra of the PFN-Br:$FcFk_2$ blend showed Fe^{2+} and Fe^{3+} species located at 708.7 and 710.0 eV for $2p_{3/2}$ and 721.9 and 723.5 eV for $2p_{1/2}$, respectively.[49,50] The following low-intensity peaks at 714.4 and 729.4 eV from fitting can be attributed to the satellite peak characteristics of Fe^{2+}/Fe^{3+} species.[50,51] The Fe^{3+} species is produced by the shifted electron density in π-π delocalized systems of Cp rings toward the electron-withdrawing C=O substituents.[52] In this case, the π electrons of Cp rings are withdrawn, and electron-back donation occurs from the Fe center to Cp rings, partially inducing a higher oxidation state of Fe (2+ to 3+).[53,54] This is consistent with the evidence of O 1*s* and Fe 2*p* XPS spectra, confirming the formation of a CT complex between PFN-Br and $FcFk_2$, in agreement with the theoretical prediction. Furthermore, Fourier transform infrared (FT-IR) absorption spectra were demonstrated in Figure S19. The close-up image of FT-IR profiles reveals the peak shift of hybrid ETL (centered at 1,564 cm^{-1}) compared to $FcFk_2$ (shown at 1,568 cm^{-1}). This peak of $FcFk_2$, which refers to C=C stretching of the furan ring, does not overlap with the PFN-Br spectrum,[55,56] suggesting the formation of a ground-state CT.[57] This is correlated with the O 1*s* core-level XPS spectra in Figure 2A showing the lower BE of the furan moiety in PFN-Br:$FcFk_2$ and concurrent to the DFT calculations, which illustrates the strong vdW interaction between the fluorene in PFN-Br and the furan of $FcFk_2$.

We then performed XPS investigations on PFN-Br and PFN-Br:$FcFk_2$ (2.5 mol%) films deposited on 100 nm Ag to reveal the origin of the reduced work function induced by the complex. The survey scans of Ag, PFN-Br, and PFN-Br:$FcFk_2$ are depicted in Figure S20. All other scans, e.g., C 1*s*, O 1*s*, and Br 3*d* narrow scans, are shown in Figure S21. The N 1*s* core-level spectra in Figure 2C show two peaks associated with N^+ and N–C for higher and lower BE, respectively.[16,58] Upon $FcFk_2$ mixing, the BE of N–C shifts toward lower values compared with pristine PFN-Br, indicating weakened interactions with Br^- anions and an increase in interactions between N and the Ag metal.[16,59] In previous reports,[60,61] the N-containing group plays a pivotal role in decreasing the work function of metal by generating interfacial dipoles, which produce high electron density on the Ag surface. Hence, in Figure 2D, we observed the lower BE of Ag 3*d* from PFN-Br:$FcFk_2$ (367.7 eV) compared with PFN-Br (367.9 eV). The Ag 3*s* core-level profiles also elucidate the same manner as 3*d* region (Figure S22), which conclusively underpins the process of reducing the Ag work function induced by the complex PFN-Br:$FcFk_2$.

The topography of ETLs on indium tin oxide (ITO)/PEDOT:PSS/PM6:BTP-eC9 was examined by atomic force microscopy (AFM) with non-contact mode. In Figure 2E, PFN-Br and hybrid ETL elucidate similar surface morphology, in contrast with the BHJ layer, which showed a fibril-like profile. Figure 2F depicts the histogram of surface height evaluated from AFM images. The PFN-Br:$FcFk_2$ ETL forms a uniform distribution with root-mean-square roughness (σ_{rms}) of 1.08 nm compared with that of pure ETL (1.42 nm), suggesting favorable film formation.[62] Contact angle measurements were also employed to evaluate the wettability of hybrid ETLs on the BHJ interface.

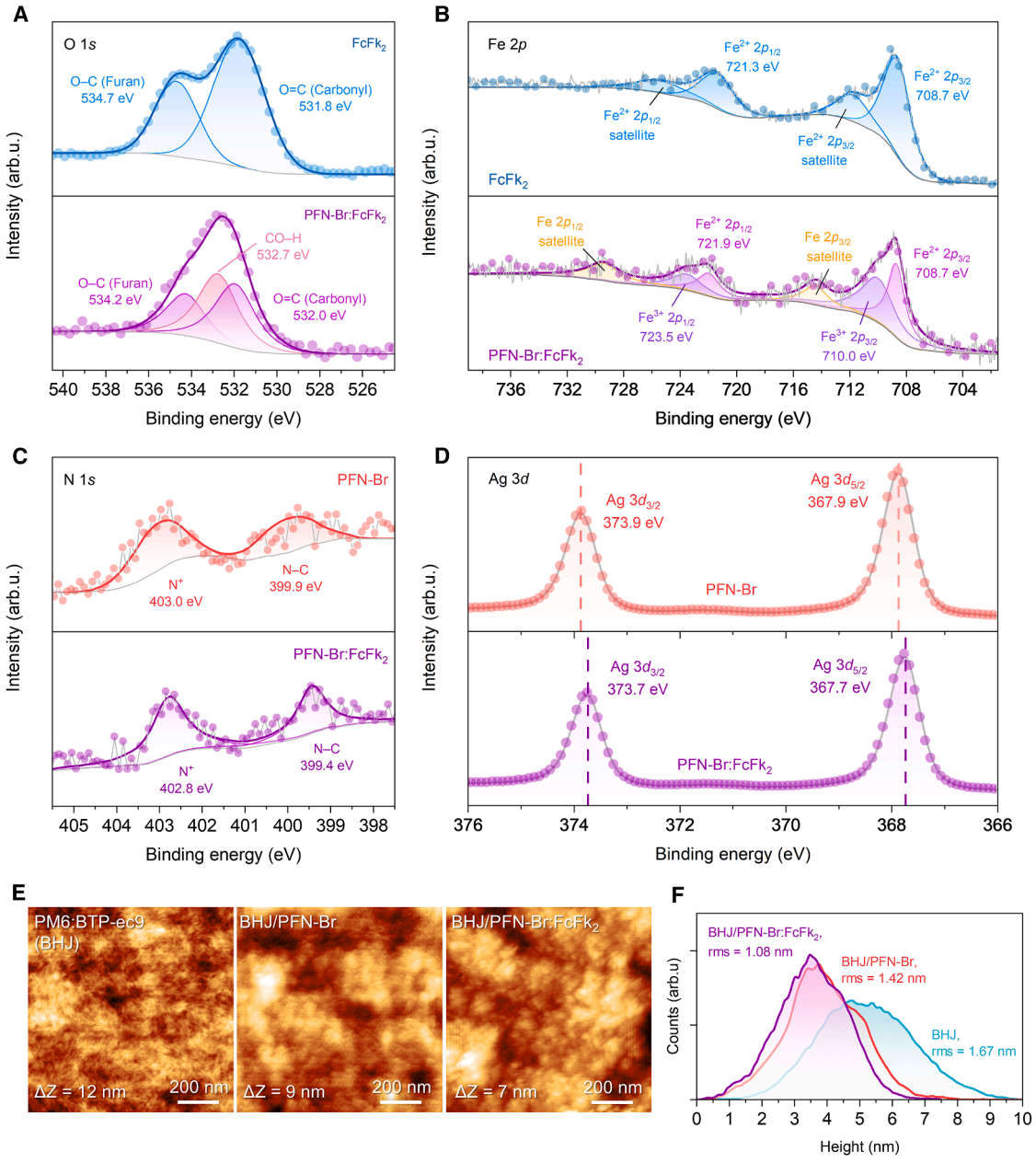

Figure 2. Elemental species and interfaces

(A and B) O 1*s* and Fe 2*p* XPS core-level profiles of pure $FcFk_2$ and PFN-Br:$FcFk_2$ (50 mol%). The dots or dots with light gray lines in the XPS spectra are raw data, and the solid lines are fitting curves.

(C and D) N 1*s* and Ag 3*d* XPS core-level spectra from PFN-Br:$FcFk_2$ and pristine PFN-Br films on Ag electrodes. The dots and lines are described as above.

(E and F) AFM images and surface height distribution of ITO/PEDOT:PSS/PM6:BTP-eC9 (as BHJ), BHJ/PFN-Br, and BHJ/PFN-Br:$FcFk_2$, respectively.

Figure S23 depicted the contact angle images for each ETL extracted from the same stacks used in the AFM measurements. The PFN-Br:$FcFk_2$ ETL showed the improved dispersion with a contact angle of 12.43°. Meanwhile, PFN-Br features a higher contact angle of 38.66°. AFM and contact angle measurements indicate that the hybrid ETL established better interfacial contact with the BHJ, therefore facilitating charge transport and extraction.[10,24,63]

Performance of OSCs with various ETLs

To compare the photovoltaic performance of PFN-Br:Fc-derived ETLs, PM6 and BTP-eC9 were selected as donor and acceptor materials, respectively, using the conventional device geometry of ITO/PEDOT:PSS/PM6:BTP-eC9/ETL/Ag (Figure 3A). The concentration of $FcFk_2$ was carefully optimized, the results of which are summarized in Figure S24 and Table S5. Additionally, we also employed pristine $FcFk_2$ as an ETL. However, the

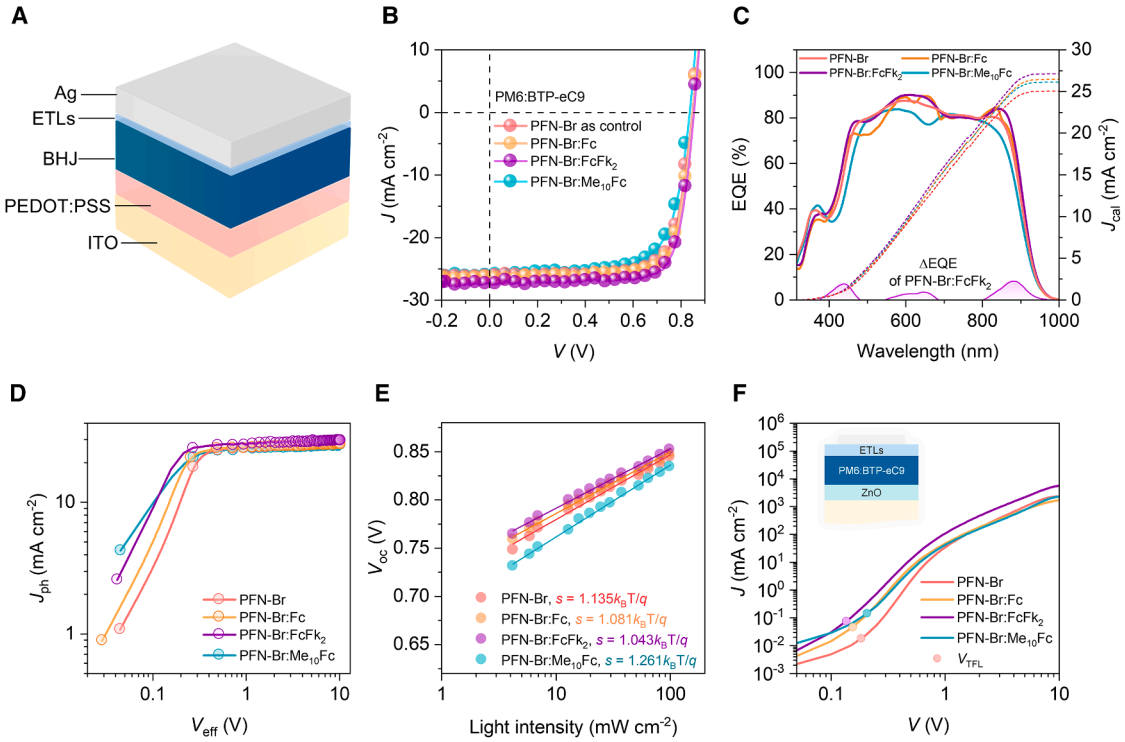

Figure 3. Device characteristics

(A) The OSC structure for a conventional architecture.

(B) The *J-V* characteristic curves under AM1.5G illumination.

(C) EQE spectra of OSC devices with various ETLs.

(D) Photocurrent density as a function of effective voltage at 100 mW cm^{-2} condition.

(E) The plots of light intensity-dependent V_{oc}.

(F) The *J-V* curves of electron-only devices with various ETLs. Solid circles in every curve are the trap-filled limit voltage (V_{TFL}).

performance of this device was poor due to the mismatch of energetics between $FcFk_2$ and BTP-eC9 (Figure S25). Figure 3B shows the current density-voltage (*J-V*) characteristic curves under AM1.5G illumination, with the detailed device parameters provided in Table 1. The statistics of the parameters are depicted in Figure S26. The PFN-Br devices used as reference cells delivered an average PCE of 17.1%, with a short-circuit current density (J_{sc}) of 26.6 mA cm^{-2}, an open-circuit voltage (V_{oc}) of 0.850 V, and a FF of 75.6%, which is in line with previous reports.[8,12,64] Notably, the PFN-Br:$FcFk_2$ devices delivered higher FF values of 77.3%, V_{oc} of 0.856 V, and J_{sc} of 27.3 mA cm^{-2}, leading to an overall increased average PCE of 18.2% (18.5% for champion OSCs). OSC devices from PFN-Br:Fc also demonstrated an enhancement of J_{sc} and FF of 26.8 mA cm^{-2} and 77.1%, respectively, with an average PCE of 17.6%. However, PFN-Br:$Me_{10}Fc$ ETL cells showed lower J_{sc} (25.8 mA cm^{-2}), V_{oc} (0.838 V), and FF (72.1%), leading to an average PCE of 15.6%. This can be ascribed to mismatched energetics resulting from the deeper LUMO level of $Me_{10}Fc$ due to the ten electron-donating methyl groups on the Cp rings. Improved alignment between the work function and the LUMO of BTP-eC9 enhances charge selectivity, thereby boosting overall photovoltaic parameters.[17,18]

The higher J_{sc} in the $FcFk_2$-mixed ETL is confirmed by external quantum efficiency (EQE) measurements (Figure 3C). The integrated photocurrent density (J_{cal}) is calculated from the EQE spectra, which is in good agreement (±3%) with the J_{sc} values shown in Table 1. Compared to the PFN-Br reference devices, the PFN-Br:$FcFk_2$ ETL enhances the overall light-to-current

Table 1. Photovoltaic parameters of OSCs based on PM6:BTP-eC9 upon different ETLs

ETLs	PCE (%)[a]	J_{sc} (mA cm^{-2})	V_{oc} (V)	FF (%)	J_{cal} (mA cm^{-2})
PFN-Br	17.2 (17.1 ± 0.3)	26.5 (26.6 ± 0.4)	0.851 (0.850 ± 0.003)	76.6 (75.6 ± 0.7)	26.2
PFN-Br:Fc	17.8 (17.6 ± 0.3)	27.0 (26.8 ± 0.4)	0.851 (0.852 ± 0.003)	77.1 (77.1 ± 0.6)	26.4
PFN-Br:$FcFk_2$	18.3 (18.1 ± 0.2)	27.2 (27.3 ± 0.3)	0.854 (0.856 ± 0.003)	78.5 (77.6 ± 0.4)	27.1
PFN-Br:$Me_{10}Fc$	16.5 (15.6 ± 0.6)	26.4 (25.8 ± 0.7)	0.843 (0.838 ± 0.005)	74.4 (72.1 ± 1.5)	25.1

[a]Average values with standard deviations in parentheses are obtained from 15 independent cells.

conversion, as shown by $\Delta EQE = EQE_{FcFk_2} - EQE_{reference}$. Meanwhile, the PFN-Br:$Me_{10}Fc$ ETL decreases the overall EQE response and consequently results in lower J_{sc}. The higher photoresponse in $FcFk_2$-based devices is attributed to more efficient carrier extraction and transport. To understand exciton dissociation and charge collection efficiency, the photocurrent density (J_{ph}) as a function of effective voltage (V_{eff}) was plotted in Figure 3D. J_{ph} is quantified by $J_{ph} = J_L - J_D$, where J_L and J_D are current densities under 1 sun irradiation and darkness, respectively. V_{eff} is defined as $V_{eff} = V_O - V$, where V_O is a compensation voltage ($J_{ph}(V_O) = 0$) and V is a bias voltage.[65] Overall, the J_{ph} for all cells reached saturation for $V_{eff} < 1$ V. This suggests that all generated excitons (electron-hole pairs) are dissociated into free charge carriers and extracted by electrodes. In the saturated regime, we can evaluate the maximum generation rate (G_{max}) from $J_{sat} = qG_{max}L$, where J_{sat} is the saturated current density, q is the elementary charge, and L is the active layer thickness. The calculated G_{max} are 1.74×10^{21}, 1.75×10^{21}, 1.80×10^{21}, and 1.74×10^{21} cm^{-3} s^{-1} for PFN-Br, PFN-Br:Fc, PFN-Br:$FcFk_2$, and PFN-Br:$Me_{10}Fc$, respectively. The significant improvement is shown by the charge generation rate under maximum power point (mpp), G_{mpp}, and short-circuit, G_{sc}, conditions estimated by the ratio of J_{ph}/J_{sat}. At V_{mpp}, the G_{mpp} of the PFN-Br:$FcFk_2$ device exhibits the highest value of 89.5% compared with the reference cell (85.1%), PFN-Br:Fc (86.2%), and PFN-Br:$Me_{10}Fc$ (74.7%). Moreover, the same trend can be observed in G_{sc}, where all values are summarized in Table S6. The higher G_{mpp} and G_{sc} values indicate better charge collection and exciton dissociation efficiency with the aid of hybrid ETLs, which aligns well with the EQE spectra.

We also measured J-V characteristics at various light intensities (P_{light}) to understand recombination processes in the devices. The relationship between J_{sc} and P_{light} follows the power law, which is $J_{sc} \propto (P_{light})^{\alpha}$, where α is the power factor. When J_{sc} is linearly dependent on P_{light} ($\alpha \approx 1$), most of the generated carriers are collected, i.e., minor or no bimolecular recombination, albeit deterioration exists with $\alpha < 1$.[66] All fabricated ETL devices demonstrated similar α values in the range of 0.933–0.965, indicating low bimolecular recombination in charge extraction processes (Figure S27). On the other hand, the degree of trap-assisted recombination can be revealed by plotting V_{oc} versus the natural logarithm of P_{light} in Figure 3E. The slope (s) is expressed in the form of nk_BT/q, where n is the recombination ideality factor, k_B is the Boltzmann constant, and T is the temperature. A slope with $n = 1$ is correlated to trap-free charge transport, whereas the case with $n = 2$ is usually associated with trap-assisted across the active layer and interfaces.[67] Compared to all the OSC devices, hybrid $FcFk_2$-based OSCs show the lowest slope of 1.043 k_BT/q, while reference devices obtain a slope of 1.135 k_BT/q. Thus, the addition of $FcFk_2$ to PFN-Br can considerably reduce trap-induced recombination. We also performed drift-diffusion simulations of J-V curves measured under different illumination intensities, while the parameters of the simulation are summarized in Table S7.[68,69] The fitting results (see Table S8) shown in Figure S28 pointed to lower series resistance, higher charge generation, and lower recombination for the devices with the PFN-Br:$FcFk_2$. The space-charge limited current (SCLC) technique for electron-only devices was carried out to study the trap-filled limited voltage (V_{TFL}).[70,71] In Figure 3F, the PFN-Br:$FcFk_2$ and PFN-Br:Fc ETLs show lower V_{TFL} of 0.136 and 0.150 V, respectively, compared with the reference (0.184 V), albeit the V_{TFL} of the PFN-Br:$Me_{10}Fc$ ETL obtained a higher value of 0.207 V. The suppression of V_{TFL} corresponds to the reduction of defects at the interfaces through the use of hybrid ETLs.

Carrier dynamics, photostability, and versatile improvement of hybrid ETLs

Capacitance-voltage (C-V) measurements were used to investigate the charge carrier transport in PM6:BTP-eC9 systems with different ETLs and conducted at V_{oc} under 1 sun intensity. From the equivalent circuit model, depicted in the inset in Figure 4A, we can extract the recombination resistance (R_{rec}) and transport resistance (R_t), which are respectively parallel to chemical capacitance (C_μ) and geometry capacitance (C_g), while R_S is the series resistance.[72] The Nyquist plot (Figure 4A) was acquired from the impedance spectra of PFN-Br and PFN-Br:$FcFk_2$ ETLs, and the overall results are summarized in Figure S29 and Table S9. The hybrid ETLs formed with Fc and $FcFk_2$ exhibit a lower R_{rec} than pristine PFN-Br cells. Meanwhile, the R_{rec} of the PFN-Br:$Me_{10}Fc$ ETL dramatically increased. Subsequently, we calculated the charge carrier lifetime (τ) by the formula $\tau = (R_{rec})(C_\mu)$. The PFN-Br:$FcFk_2$, PFN-Br:Fc, and PFN-Br series show similar charge carrier lifetimes of 1.46, 1.80, and 2.17 μs, respectively. However, the PFN-Br:$Me_{10}Fc$ ETL features a higher τ of 6.17 μs, which can be ascribed to the formation of more interface trap-state densities or a mismatch between the energetics of the BHJ and electron extraction layers, leading to a larger recombination at the interface between the two layers.[73] Interestingly, the R_t of PFN-Br:$FcFk_2$ cells significantly decreased to 32.9 Ω compared with reference devices (57.5 Ω). This evidence can strongly confirm the better charge extraction and transport process from the BHJ/ETL to Ag contact, which can improve V_{oc} and FF.[18,62] The Mott-Schottky analysis was used to elucidate the C-V relationship of $1/C^2 = (2/q\varepsilon_o\varepsilon_r N_A A^2)(V - V_{bi})$, where ε_o is the dielectric constant in free space, ε_r is the relative dielectric constant, N_A is doping concentration, A is the active area of the device, and V_{bi} is the built-in potential.[8,72] In Figure 4B, the Mott-Schottky characteristics of the $FcFk_2$ hybrid ETL and PFN-Br cells are plotted by measuring under direct current (DC) bias at 10 KHz. The V_{bi} extracted from the x-intercept in Figure 4B are 0.818 and 0.837 V for PFN-Br and PFN-Br:$FcFk_2$ devices, respectively. The greater V_{bi} of the hybrid ETL is ascribed to better Ohmic contact between the BHJ and ETL, facilitating the improvement of V_{oc}.[74] Transient photocurrent (TPC) measurements were carried out to study the charge carrier dynamics (Figure 4C). The PFN-Br:$FcFk_2$ ETL demonstrated a faster photocurrent decay (53.2 ns) compared with the decay time of reference cells (176.5 ns), indicating faster charge extraction enabled by the incorporation of $FcFk_2$.

Despite the high PCE reported for $FcFk_2$-based OSCs, studying their photostability under operating conditions is pivotal to demonstrating the real-world applicability of these devices. The unencapsulated PM6:BTP-eC9 devices with

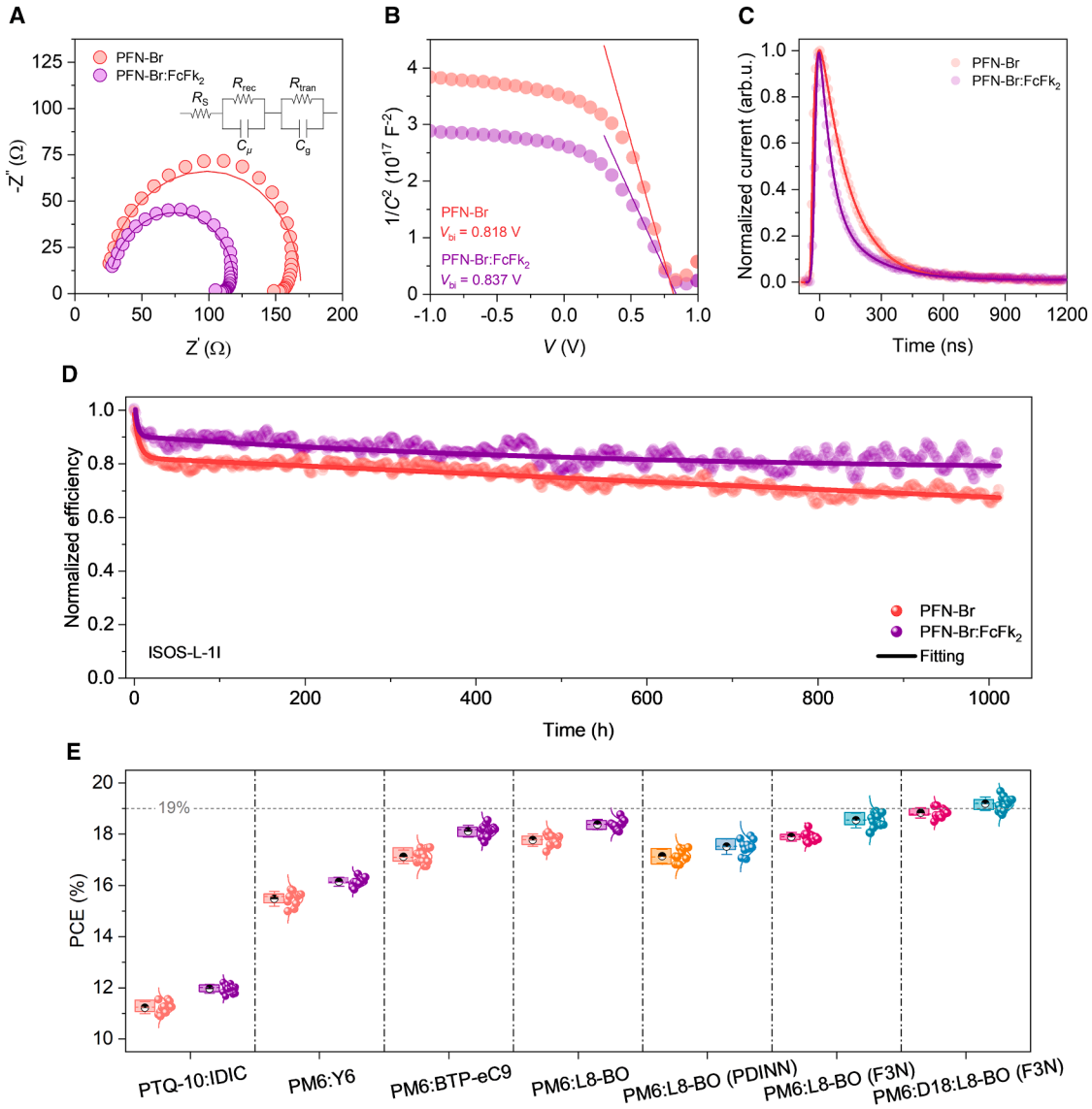

Figure 4. Device physics, stability, and universality

(A) Nyquist plots of hybrid and pristine ETLs under 1 sun illumination at V_{oc} (the inset is the equivalent circuit used for fitting).

(B) Mott-Schottky plots at 10 KHz.

(C) Transient photocurrent (TPC) decay of PFN-Br:$FcFk_2$ and reference devices.

(D) Long-term stability obtained by mpp tracking under 100 mW cm^{-2} illumination within a N_2-filled chamber.

(E) Statistics of PCE in various systems (different donors and acceptors) averaged by at least 10 devices. For the boxplot parameters, the center dashed lines, top edges, and bottom edges are the median, 75th percentile, and 25th percentile, respectively. The white-black circles are the mean values, and the whiskers show the standard deviations. The red and purple data are PFN-Br and PFN-Br:$FcFk_2$, respectively. The orange spheres are PDINN, and the blue spheres are PDINN:$FcFk_2$. The magenta and cyan color spheres are referred to as exploiting PNDIT-F3N (abbreviated to F3N) as an ETL for the reference and PNDIT-F3N:$FcFk_2$, respectively.

PFN-Br and PFN-Br:$FcFk_2$ ETLs were loaded in a N_2-filled chamber and tracked at mpp under AM1.5G illumination following the ISOS-L-1I protocol, i.e., ambient temperature and humidity in an inert (N_2) atmosphere, depicted in Figure 4D.[75] Both devices showed burn-in features, which can be ascribed to thermal instability and photo-induced trap states.[76] The $FcFk_2$-hybrid ETL-based OSCs retain performance at >80% of their initial PCE up to 700 h, while the reference devices drop to <70% of their initial values. We attributed the longer device stability to the decreased trap-assisted recombination and less Fermi level pinning, which effectively facilitates charge extraction in $FcFk_2$-based OSCs.[58,77] To better understand the superior stability in the hybrid ETL-based devices, we performed temperature and light intensity dependent *J-V* characterizations[78] for fresh and aged devices, depicted in Figures S30 and S31 and Figures S32 and S33,

respectively. Figure S34 showed the Urbach energy (E_U) as a function of V_{oc} for fresh and aged samples at different light intensities. Notably, the E_U of reference devices shows a higher shift after degradation compared with that of PFN-Br:$FcFk_2$. This suggests higher interface recombination upon degradation in the reference devices,[79] which confirms the improved photostability in PFN-Br:$FcFk_2$ hybrid ETLs.

Finally, we demonstrated the generality of the novel CT complex formation between $FcFk_2$ and ETL with various polymer donors and NFAs. PM6, D18, and PTQ-10 were selected in combination with L8-BO, BTP-eC9, Y6, and IDIC as acceptors, with LUMO values ranging from −3.90 to −4.13 eV.[17,80–82] The chemical structures of the materials are shown in Figure S35. The PCE box plots of various donor:acceptor (D:A) systems with the ETLs of PFN-Br and PFN-Br:$FcFk_2$ are depicted in Figure 4E. The PFN-Br:$FcFk_2$-based systems show an overall improved performance compared with the reference devices for all D:A blends, of which photovoltaic curves and EQE spectra are respectively demonstrated in Figures S36 and S37. The photovoltaic parameters are collected in Table S10. For the PM6:L8-BO blend, PFN-Br:$FcFk_2$ devices delivered a PCE of 18.8% for the champion device. Meanwhile, the PFN-Br-based reference cells show a maximum PCE of 18.1%. Moreover, we tested the same protocol for different ETLs. In particular, we chose PNDIT-F3N as the ETL and PM6:L8-BO and PM6:D18:L8-BO (ternary) as the photoactive layers. *J-V* characteristics, EQE spectra, and *J-V* parameters are depicted in Figure S38 and Table S11. The PM6:L8-BO devices employing the PNDIT-F3N:$FcFk_2$ ETL can achieve a maximum PCE of 18.9% compared with the reference cells (18.3%). For the ternary system, the reference devices exhibited an average PCE of 18.6%, a J_{sc} of 26.2 mA cm^{-2}, a V_{oc} of 0.903 V, and an FF of 79.0%. Notably, the hybrid ETL-based ternary devices using $FcFk_2$ delivered the highest PCE of 19.7%, with a J_{sc} of 27.1 mA cm^{-2}, a V_{oc} of 0.907 V, and an FF of 80.1%. Upon addition of an antireflective coating, the PCE was further improved to 20.1% (Figure S39). For PDINN-based devices (PM6:L8-BO), PDINN:$FcFk_2$ also elucidated the improvement in FF to yield a PCE of 17.9% compared with reference cells (17.5%). The universal improvements of versatile D:A systems and ETLs strongly highlight the promising tuning procedure for ETLs. With the correct functionalization of Fc-derived compounds, state-of-the-art OSCs can be anticipated to surpass current robustness and light-harvesting performance.

Conclusions

In summary, we have introduced a simple route toward low-cost Fc-functionalized OSCs. These have been obtained via CT complex formation between $FcFk_2$ and polymer ETLs, as demonstrated by optoelectronic measurements and DFT calculations. PFN-Br:$FcFk_2$ ETL can modify the work function of Ag from −4.50 to −4.03 eV, which in turn enhances the FF. To this end, the $FcFk_2$ hybrid ETL successfully delivered efficient OSCs based on PM6:BTP-eC9, yielding a PCE of 18.5%. The electrical and device physics characterizations crucially underpin the high photovoltaic efficiency benefiting from reduced trap-assisted recombination and faster charge extraction. Stability measurements were conducted to show the robustness of hybrid ETL cells, which retain 80% of PCE up to 700 h. Moreover, the versatility of D:A systems and ETLs demonstrates the universal improvement when using $FcFk_2$ molecules, i.e., delivering a PCE of 20.1%. The functionalization of organic semiconductors with hybrid ETLs incorporating $FcFk_2$ highlights a rational approach for the molecular design of Fc derivatives aimed at enhancing charge extraction and, consequently, improving light-to-current conversion efficiency.

RESOURCE AVAILABILITY

Lead contact

Further information and requests for resources and materials should be directed to and will be fulfilled by the lead contact, Nicola Gasparini (n.gasparini@imperial.ac.uk).

Materials availability

All materials generated in this study are available from the lead contact with reasonable requirements.

Data and code availability

All data are present in the paper and supplemental information. Other data are available from the lead contact or corresponding author.

Full details of experimental procedures can be found in the supplemental information.

ACKNOWLEDGMENTS

N.G. thanks the Engineering and Physics Science Research Council (EPSRC) (EP/T028513/1) and the European Union under grant agreement number 101172797. P.P. acknowledges funding support from the National Science, Research and Innovation Fund (NSRF) via the Program Management Unit for Human Resources and Institutional Development, Research and Innovation (grant number B49G680107). N.J.L. acknowledges Imperial College London for funding via the Sir Edward Frankland BP Chair endowment, Impact Acceleration Award, and the Deep-Tech Prime program and is also grateful for a Royal Society Wolfson Research Merit award. P.S. acknowledges C. Kaiyasuan for helping with PL measurements.

AUTHOR CONTRIBUTIONS

N.G. and N.J.L. conceived the ideas and supervised the project. P.S., W.D.J.T., and Z.Q. performed the investigation and characterization of the Fc derivatives and solar cell fabrication. C.C. and S.I. performed XPS measurements under the supervision of P.P. E.H. and B.H. measured the transient measurements under the supervision of A.B. K.F. performed electrical modeling under the supervision of C.J.B. J.H. performed the DFT calculation under the supervision of D.B. L.L. supported the cryostage operation. F.V. and Z.Z. supported with device fabrication. P.S. wrote the manuscript. P.S., W.D.J.T., Z.Q., N.G., and N.J.L. revised the manuscript. All authors discussed the results and commented on the final manuscript.

DECLARATION OF INTERESTS

The authors declare no competing interests.

SUPPLEMENTAL INFORMATION

Supplemental information can be found online at https://doi.org/10.1016/j.joule.2025.102107.

Received: January 3, 2025
Revised: March 5, 2025
Accepted: August 11, 2025
Published: September 5, 2025

REFERENCES

1. Bihar, E., Corzo, D., Hidalgo, T.C., Rosas-Villalva, D., Salama, K.N., Inal, S., and Baran, D. (2020). Fully Inkjet-Printed, Ultrathin and Conformable Organic Photovoltaics as Power Source Based on Cross-Linked PEDOT:PSS Electrodes. Adv. Mater. Technol. *5*, 2000226. https://doi.org/10.1002/admt.202000226.

2. Panidi, J., Mazzolini, E., Eisner, F., Fu, Y., Furlan, F., Qiao, Z., Rimmele, M., Li, Z., Lu, X., Nelson, J., et al. (2023). Biorenewable Solvents for High-Performance Organic Solar Cells. ACS Energy Lett. *8*, 3038–3047. https://doi.org/10.1021/acsenergylett.3c00891.

3. Corzo, D., Rosas-Villalva, D., C, A., Tostado-Blázquez, G., Alexandre, E. B., Hernandez, L.H., Han, J., Xu, H., Babics, M., De Wolf, S., et al. (2023). High-performing organic electronics using terpene green solvents from renewable feedstocks. Nat. Energy *8*, 62–73. https://doi.org/10.1038/s41560-022-01167-7.

4. Zhu, L., Zhang, M., Zhou, G., Wang, Z., Zhong, W., Zhuang, J., Zhou, Z., Gao, X., Kan, L., Hao, B., et al. (2024). Achieving 20.8% organic solar cells via additive-assisted layer-by-layer fabrication with bulk p-i-n structure and improved optical management. Joule *8*, 3153–3168. https://doi.org/10.1016/j.joule.2024.08.001.

5. Jiang, Y., Sun, S., Xu, R., Liu, F., Miao, X., Ran, G., Liu, K., Yi, Y., Zhang, W., and Zhu, X. (2024). Non-fullerene acceptor with asymmetric structure and phenyl-substituted alkyl side chain for 20.2% efficiency organic solar cells. Nat. Energy *9*, 975–986. https://doi.org/10.1038/s41560-024-01557-z.

6. Li, Y., Huang, X., Ding, K., Sheriff, H.K.M., Ye, L., Liu, H., Li, C.Z., Ade, H., and Forrest, S.R. (2021). Non-fullerene acceptor organic photovoltaics with intrinsic operational lifetimes over 30 years. Nat. Commun. *12*, 5419. https://doi.org/10.1038/s41467-021-25718-w.

7. Yip, H.L., and Jen, A.K.Y. (2012). Recent advances in solution-processed interfacial materials for efficient and stable polymer solar cells. Energy Environ. Sci. *5*, 5994–6011. https://doi.org/10.1039/c2ee02806a.

8. Fan, B., Gao, H., Li, Y., Wang, Y., Zhao, C., Lin, F.R., and Jen, A.K.Y. (2024). Integration of polyoxometalate clusters with self-assembled monolayer for efficient and robust organic solar cells. Joule *8*, 1443–1456. https://doi.org/10.1016/j.joule.2024.03.009.

9. Troughton, J., Neophytou, M., Gasparini, N., Seitkhan, A., Isikgor, F.H., Song, X., Lin, Y.H., Liu, T., Faber, H., Yengel, E., et al. (2020). A universal solution processed interfacial bilayer enabling ohmic contact in organic and hybrid optoelectronic devices. Energy Environ. Sci. *13*, 268–276. https://doi.org/10.1039/C9EE02202C.

10. Jiang, Y., Dong, X., Sun, L., Liu, T., Qin, F., Xie, C., Jiang, P., Hu, L., Lu, X., Zhou, X., et al. (2022). An alcohol-dispersed conducting polymer complex for fully printable organic solar cells with improved stability. Nat. Energy *7*, 352–359. https://doi.org/10.1038/s41560-022-00997-9.

11. Yaacobi-Gross, N., Treat, N.D., Pattanasattayavong, P., Faber, H., Perumal, A.K., Stingelin, N., Bradley, D.D.C., Stavrinou, P.N., Heeney, M., and Anthopoulos, T.D. (2015). High-efficiency organic photovoltaic cells based on the solution-processable hole transporting interlayer copper thiocyanate (CuSCN) as a replacement for PEDOT:PSS. Adv. Energy Mater. *5*, 1401529. https://doi.org/10.1002/aenm.201401529.

12. Lin, Y., Firdaus, Y., Isikgor, F.H., Nugraha, M.I., Yengel, E., Harrison, G.T., Hallani, R., El-Labban, A., Faber, H., Ma, C., et al. (2020). Self-assembled monolayer enables hole transport layer-free organic solar cells with 18% efficiency and improved operational stability. ACS Energy Lett. *5*, 2935–2944. https://doi.org/10.1021/acsenergylett.0c01421.

13. Al-Ashouri, A., Magomedov, A., Roß, M., Jošt, M., Talaikis, M., Chistiakova, G., Bertram, T., Márquez, J.A., Köhnen, E., Kasparavičius, E., et al. (2019). Conformal monolayer contacts with lossless interfaces for perovskite single junction and monolithic tandem solar cells. Energy Environ. Sci. *12*, 3356–3369. https://doi.org/10.1039/C9EE02268F.

14. Huang, F., Wu, H., Wang, D., Yang, W., and Cao, Y. (2004). Novel Electroluminescent Conjugated Polyelectrolytes Based on Polyfluorene. Chem. Mater. *16*, 708–716. https://doi.org/10.1021/cm034650o.

15. Wu, Z., Sun, C., Dong, S., Jiang, X.F., Wu, S., Wu, H., Yip, H.L., Huang, F., and Cao, Y. (2016). N-Type Water/Alcohol-Soluble Naphthalene Diimide-Based Conjugated Polymers for High-Performance Polymer Solar Cells. J. Am. Chem. Soc. *138*, 2004–2013. https://doi.org/10.1021/jacs.5b12664.

16. Feng, C., Wang, X., He, Z., and Cao, Y. (2021). Formation Mechanism of PFN Dipole Interlayer in Organic Solar Cells. Sol. RRL *5*, 2000753. https://doi.org/10.1002/solr.202000753.

17. Liu, L., Chen, S., Qu, Y., Gao, X., Han, L., Lin, Z., Yang, L., Wang, W., Zheng, N., Liang, Y., et al. (2021). Nanographene–Osmapentalyne Complexes as a Cathode Interlayer in Organic Solar Cells Enhance Efficiency over 18%. Adv. Mater. *33*, e2101279. https://doi.org/10.1002/adma.202101279.

18. Lai, X., Chen, S., Gu, X., Lai, H., Wang, Y., Zhu, Y., Wang, H., Qu, J., Kyaw, A.K.K., Xia, H., et al. (2023). Phenanthroline-carbolong interface suppress chemical interactions with active layer enabling long-time stable organic solar cells. Nat. Commun. *14*, 3571. https://doi.org/10.1038/s41467-023-39223-9.

19. Ye, L., Cai, Y., Li, C., Zhu, L., Xu, J., Weng, K., Zhang, K., Huang, M., Zeng, M., Li, T., et al. (2020). Ferrocene as a highly volatile solid additive in non-fullerene organic solar cells with enhanced photovoltaic performance. Energy Environ. Sci. *13*, 5117–5125. https://doi.org/10.1039/D0EE02426K.

20. Li, B., Gao, D., Sheppard, S.A., Tremlett, W.D.J., Liu, Q., Li, Z., White, A.J. P., Brown, R.K., Sun, X., Gong, J., et al. (2024). Highly Efficient and Scalable p-i-n Perovskite Solar Cells Enabled by Poly-metallocene Interfaces. J. Am. Chem. Soc. *146*, 13391–13398. https://doi.org/10.1021/jacs.4c02220.

21. Hong, E., Tremlett, W.D.J., Hart, L., Hu, B., Qiao, Z., Sukpoonprom, P., Fearn, S., Angela, E., Brunetta, M., Koutsogeorgis, D.C., et al. (2025). Ferrocene Derivatives Enable Ultrasensitive Perovskite Photodetectors with Enhanced Reverse Bias Stability. Adv. Funct. Mater. 2424556. https://doi.org/10.1002/adfm.202424556.

22. Vanin, F., Tremlett, W.D.J., Gao, D., Liu, Q., Li, B., Li, S., Gong, J., Wu, X., Li, Z., Brown, R.K., et al. (2025). Modulating Perovskite Surface Energetics Through Tuneable Ferrocene Interlayers for High-Performance Perovskite Solar Cells. Angew. Chem. Int. Ed. Engl. *64*, e202424041. https://doi.org/10.1002/anie.202424041.

23. Li, Z., Li, B., Wu, X., Sheppard, S.A., Zhang, S., Gao, D., Long, N.J., and Zhu, Z. (2022). Organometallic-functionalized interfaces for highly efficient inverted perovskite solar cells. Science *376*, 416–420. https://doi.org/10.1126/science.abm8566.

24. Chen, X., Xia, D., Li, C., Luo, C., Jiang, X., Hu, Z., Wan, L., Jiang, L., Zhao, C., and Li, W. (2024). Ferrocene-Terminated Perylene Diimide-Based Small Molecular Electrolyte as Electron-Transport Layer for Efficient Organic Solar Cells. Sol. RRL *8*, 2300823. https://doi.org/10.1002/solr.202300823.

25. Zheng, H., Hu, L., Hu, X., Li, H., Quan, J., Jin, Y., Yin, X., Song, J., Su, Z., Zhou, D., et al. (2024). Designing thickness-insensitive cathode interlayers via constructing noncovalently conformational locks for highly efficient non-fullerene organic solar cells. J. Mater. Chem. A *12*, 2413–2422. https://doi.org/10.1039/D3TA07050F.

26. Ma, L.K., Chen, Y., Chow, P.C.Y., Zhang, G., Huang, J., Ma, C., Zhang, J., Yin, H., Hong Cheung, A.M., Wong, K.S., et al. (2020). High-Efficiency Indoor Organic Photovoltaics with a Band-Aligned Interlayer. Joule *4*, 1486–1500. https://doi.org/10.1016/j.joule.2020.05.010.

27. Grimme, S., Ehrlich, S., and Goerigk, L. (2011). Effect of the damping function in dispersion corrected density functional theory. J. Comput. Chem. *32*, 1456–1465. https://doi.org/10.1002/jcc.21759.

28. Lopes, J.N.C., Do Couto, P.C., and Da Piedade, M.E.M. (2006). An all-atom force field for metallocenes. J. Phys. Chem. A *110*, 13850–13856. https://doi.org/10.1021/jp062896l.

29. Dolg, M., Wedig, U., Stoll, H., and Preuss, H. (1987). Energy-adjusted ab initio pseudopotentials for the first row transition elements. J. Chem. Phys. *86*, 866–872. https://doi.org/10.1063/1.452288.

30. Krishnan, R., Binkley, J.S., Seeger, R., and Pople, J.A. (1980). Self-consistent molecular orbital methods. XX. A basis set for correlated wave functions. J. Chem. Phys. *72*, 650–654. https://doi.org/10.1063/1.438955.

31. Méndez, H., Heimel, G., Opitz, A., Sauer, K., Barkowski, P., Oehzelt, M., Soeda, J., Okamoto, T., Takeya, J., Arlin, J.B., et al. (2013). Doping of organic semiconductors: Impact of dopant strength and electronic coupling. Angew. Chem. Int. Ed. Engl. *52*, 7751–7755. https://doi.org/10.1002/anie.201302396.

32. Ge, W., Liu, C., Xu, Y., Zhang, J., Si, W., Wang, W., Ou, C., and Dong, X. (2022). Crystal engineering of ferrocene-based charge-transfer complexes for NIR-II photothermal therapy and ferroptosis. Chem. Sci. *13*, 9401–9409. https://doi.org/10.1039/d2sc03273b.

33. Zhou, M., Jin, X., Jia, M., Quan, D., Liu, B., Wei, Y., Kong, X.Y., Wen, L., and Jiang, L. (2024). Light-Powered Directional Ion Transport via PFN-Br/MoS_2 Heterogeneous Membranes: Band Alignment and Activation Energy Barrier Engineering. ACS Appl. Mater. Interfaces *16*, 39321–39329. https://doi.org/10.1021/acsami.4c05901.

34. Tanaka, Y., Man-Chung Wong, K., and Wing-Wah Yam, V. (2012). Phosphorescent molecular tweezers based on alkynylplatinum(II) terpyridine system: Turning on of NIR emission via heterologous Pt···M interactions (M = PtII, PdII, AuIII and AuI). Chem. Sci. *3*, 1185–1191. https://doi.org/10.1039/c2sc00935h.

35. Lu, T., and Chen, Q. (2021). Interaction Region Indicator: A Simple Real Space Function Clearly Revealing Both Chemical Bonds and Weak Interactions. Chemistry. Methods *1*, 231–239. https://doi.org/10.1002/cmtd.202100007.

36. Baer, D.R. (2005). Summary of ISO/TC 201 standard: XVIII, ISO 19318:2004 – Surface chemical analysis – X-ray photoelectron spectroscopy – Reporting of methods used for charge control and charge correction. Surf. Interface Anal. *37*, 524–526. https://doi.org/10.1002/sia.2034.

37. Paintner, T., Björk, J., Du, P., Klyatskaya, S., Paszkiewicz, M., Hellwig, R., Uphoff, M., Öner, M.A., Cuniberto, E., Deimel, P.S., et al. (2019). Quantum Tunneling Mediated Interfacial Synthesis of a Benzofuran Derivative. Angew. Chem. Int. Ed. Engl. *58*, 11285–11290. https://doi.org/10.1002/ange.201904030.

38. Yang, T., Jin, Y., Wang, Y., Kong, A., Chen, Y., Zou, Y., Liu, C., Wei, G., and Yu, C. (2023). Covalent Furan-Benzimidazole-Linked Polymer Hollow Fiber Membrane for Clean and Efficient Photosynthesis of Hydrogen Peroxide. Adv. Funct. Mater. *33*, 2300714. https://doi.org/10.1002/adfm.202300714.

39. Buitendach, B.E., Erasmus, E., Conradie, J., Niemantsverdriet, J.W., Lang, H., and Swarts, J.C. (2024). Synthesis, Electrochemistry, XPS, and DFT Calculations of α-Carbon-Bonded Gold(I) Ferrocenyl- and Ruthenocenyl-Containing β-Diketonato Complexes. Organometallics *43*, 1334–1348. https://doi.org/10.1021/acs.organomet.4c00031.

40. Gupta, B., Kumar, N., Panda, K., Kanan, V., Joshi, S., and Visoly-Fisher, I. (2017). Role of oxygen functional groups in reduced graphene oxide for lubrication. Sci. Rep. *7*, 45030. https://doi.org/10.1038/srep45030.

41. Yang, D., Velamakanni, A., Bozoklu, G., Park, S., Stoller, M., Piner, R.D., Stankovich, S., Jung, I., Field, D.A., Ventrice, C.A., et al. (2009). Chemical analysis of graphene oxide films after heat and chemical treatments by X-ray photoelectron and Micro-Raman spectroscopy. Carbon *47*, 145–152. https://doi.org/10.1016/j.carbon.2008.09.045.

42. Kehrer, M., Duchoslav, J., Hinterreiter, A., Cobet, M., Mehic, A., Stehrer, T., and Stifter, D. (2019). XPS investigation on the reactivity of surface imine groups with TFAA. Plasma Process Polym. *16*, 1800160. https://doi.org/10.1002/ppap.201800160.

43. Zhou, J., Yang, P., Kots, P.A., Cohen, M., Chen, Y., Quinn, C.M., de Mello, M.D., Anibal Boscoboinik, J., Shaw, W.J., Caratzoulas, S., et al. (2023). Tuning the reactivity of carbon surfaces with oxygen-containing functional groups. Nat. Commun. *14*, 2293. https://doi.org/10.1038/s41467-023-37962-3.

44. Nie, Y., Li, Y., Li, J., Chen, L., Wang, X., Chen, T., and Cai, Z. (2024). Incorporated ferrocene-derivatives endow Ni-based MOF with high-performance for electrochemical detection. Colloids Surf. A Physicochem. Eng. Asp. *680*, 132742. https://doi.org/10.1016/j.colsurfa.2023.132742.

45. Niu, X., Mo, Z., Yang, X., Shuai, C., Liu, N., and Guo, R. (2019). Graphene-ferrocene functionalized cyclodextrin composite with high electrochemical recognition capability for phenylalanine enantiomers. Bioelectrochemistry *128*, 74–82. https://doi.org/10.1016/j.bioelechem.2019.03.006.

46. Yin, M., Guo, K., Meng, J., Wang, Y., Gao, H., and Xue, Z. (2024). Ferrocene-Based Polymer Organic Cathode for Extreme Fast Charging Lithium-Ion Batteries with Ultralong Lifespans. Adv. Mater. *36*, e2405747. https://doi.org/10.1002/adma.202405747.

47. Zhao, Y., Xu, N., Ni, M., Wang, Z., Zhu, J., Liu, J., Zhao, R., Zhang, H., Ma, Y., Li, C., et al. (2023). An In Situ Fabricated Graphene/Bipolar Polymer Hybrid Material Delivers Ultralong Cycle Life over 15 000 Cycles as a High-Performance Electrode Material. Adv. Mater. *35*, e2211152. https://doi.org/10.1002/adma.202211152.

48. Cano, A., Rodríguez-Hernández, J., Reguera, L., Rodríguez-Castellón, E., and Reguera, E. (2019). On the Scope of XPS as Sensor in Coordination Chemistry of Transition Metal Hexacyanometallates. Eur. J. Inorg. Chem. *2019*, 1724–1732. https://doi.org/10.1002/ejic.201801556.

49. Li, B., Wu, W., Zhang, T., Jiang, S., Chen, X., Zhang, G., and Zhang, X. (2017). Ferrocene particles incorporated into Zr-based metal-organic frameworks for selective phenol hydroxylation to dihydroxybenzenes. RSC Adv. *7*, 38691–38698. https://doi.org/10.1039/C7RA06917K.

50. Webb, T., Liu, X., Westbrook, R.J.E., Kern, S., Sajjad, M.T., Jenatsch, S., Jayawardena, K.D.G.I., Perera, W.H.K., Marko, I.P., Sathasivam, S., et al. (2022). A Multifaceted Ferrocene Interlayer for Highly Stable and Efficient Lithium Doped Spiro-OMeTAD-based Perovskite Solar Cells. Adv. Energy Mater. *12*, 2200666. https://doi.org/10.1002/aenm.202200666.

51. Nguyên Lê, T.N., Kondratenko, K., Arbouch, I., Moréac, A., Breton, J.C.L. Le, van Dyck, C., Cornil, J., Vuillaume, D., and Fabre, B. (2024). Electronic Properties of Electroactive Ferrocenyl-Functionalized MoS_2. J. Phys. Chem. C *128*, 7706–7722. https://doi.org/10.1021/acs.jpcc.4c00606.

52. Rosenblum, M., Banerjee, A.K., Danieli, N., Fish, R.W., and Schlatter, V. (1963). The Structure and Chemistry of Ferrocene. VII. Bridged Ferrocenes. J. Am. Chem. Soc. *85*, 316–324. https://doi.org/10.1021/ja00886a016.

53. Astruc, D. (2017). Why is Ferrocene so Exceptional? Eur. J. Inorg. Chem. *2017*, 6–29. https://doi.org/10.1002/ejic.201600983.

54. Du, C., Sheng, J., Zhong, F., He, Y., Liu, H., Sun, Y., and Dong, F. (2024). Boosting exciton dissociation and charge transfer in CsPbBr3 QDs via ferrocene derivative ligation for CO_2 photoreduction. Proc. Natl. Acad. Sci. USA *121*, e2315956121. https://doi.org/10.1073/pnas.2315956121.

55. Lam, J.Y., Shih, C.C., Lee, W.Y., Chueh, C.C., Jang, G.W., Huang, C.J., Tung, S.H., and Chen, W.C. (2018). Bio-Based Transparent Conductive Film Consisting of Polyethylene Furanoate and Silver Nanowires for Flexible Optoelectronic Devices. Macromol. Rapid Commun. *39*, e1800271. https://doi.org/10.1002/marc.201800271.

56. Burgess, S.K., Leisen, J.E., Kraftschik, B.E., Mubarak, C.R., Kriegel, R.M., and Koros, W.J. (2014). Chain Mobility, Thermal, and Mechanical Properties of Poly(ethylene furanoate) Compared to Poly(ethylene terephthalate). Macromolecules *47*, 1383–1391. https://doi.org/10.1021/ma5000199.

57. Duva, G., Beyer, P., Scholz, R., Belova, V., Opitz, A., Hinderhofer, A., Gerlach, A., and Schreiber, F. (2019). Ground-state charge-transfer interactions in donor:acceptor pairs of organic semiconductors – a spectroscopic study of two representative systems. Phys. Chem. Chem. Phys. *21*, 17190–17199. https://doi.org/10.1039/c9cp02939g.

58. Zheng, Y., Zhao, J., Liang, H., Zhao, Z., and Kan, Z. (2023). Double-Dipole Induced by Incorporating Nitrogen-Bromine Hybrid Cathode Interlayers

Leads to Suppressed Current Leakage and Enhanced Charge Extraction in Non-Fullerene Organic Solar Cells. Adv. Sci. (Weinh) *10*, e2302460. https://doi.org/10.1002/advs.202302460.

59. Feng, C., Wang, X., Chen, G., Zhang, B., He, Z., and Cao, Y. (2021). Mechanism of the Alcohol-Soluble Ionic Organic Interlayer in Organic Solar Cells. Langmuir *37*, 4347–4354. https://doi.org/10.1021/acs.langmuir.1c00413.
60. Sharma, A., Singh, S., Song, X., Rosas Villalva, D., Troughton, J., Corzo, D., Toppare, L., Gunbas, G., Schroeder, B.C., and Baran, D. (2021). A Nonionic Alcohol Soluble Polymer Cathode Interlayer Enables Efficient Organic and Perovskite Solar Cells. Chem. Mater. *33*, 8602–8611. https://doi.org/10.1021/acs.chemmater.1c01430.
61. Hu, L., Wu, F., Li, C., Hu, A., Hu, X., Zhang, Y., Chen, L., and Chen, Y. (2015). Alcohol-Soluble n-Type Conjugated Polyelectrolyte as Electron Transport Layer for Polymer Solar Cells. Macromolecules *48*, 5578–5586. https://doi.org/10.1021/acs.macromol.5b01137.
62. Seitkhan, A., Neophytou, M., Kirkus, M., Abou-Hamad, E., Hedhili, M.N., Yengel, E., Firdaus, Y., Faber, H., Lin, Y., Tsetseris, L., et al. (2019). Use of the Phen-NaDPO:$Sn(SCN)_2$ Blend as Electron Transport Layer Results to Consistent Efficiency Improvements in Organic and Hybrid Perovskite Solar Cells. Adv. Funct. Mater. *29*, 1905810. https://doi.org/10.1002/adfm.201905810.
63. Feng, L., Xiang, Y., Li, Z., Li, Q., Dong, H., Yan, S., Xu, B., and Hou, J. (2024). Non-ionic Perylene-Diimide Polymer as Universal Cathode Interlayer for Conventional, Inverted, and Blade-Coated Organic Solar Cells. Angew. Chem. Int. Ed. Engl. *63*, e202410857. https://doi.org/10.1002/anie.202410857.
64. Peng, W., Lin, Y., Jeong, S.Y., Firdaus, Y., Genene, Z., Nikitaras, A., Tsetseris, L., Woo, H.Y., Zhu, W., Anthopoulos, T.D., et al. (2021). Using Two Compatible Donor Polymers Boosts the Efficiency of Ternary Organic Solar Cells to 17.7%. Chem. Mater. *33*, 7254–7262. https://doi.org/10.1021/acs.chemmater.1c01433.
65. Gasparini, N., Salvador, M., Heumueller, T., Richter, M., Classen, A., Shrestha, S., Matt, G.J., Holliday, S., Strohm, S., Egelhaaf, H.J., et al. (2017). Polymer:Nonfullerene Bulk Heterojunction Solar Cells with Exceptionally Low Recombination Rates. Adv. Energy Mater. *7*, 1701561. https://doi.org/10.1002/aenm.201701561.
66. Mihailetchi, V.D., Wildeman, J., and Blom, P.W. (2005). Space-charge limited photocurrent. Phys. Rev. Lett. *94*, 126602. https://doi.org/10.1103/PhysRevLett.94.126602.
67. Cowan, S.R., Roy, A., and Heeger, A.J. (2010). Recombination in polymer-fullerene bulk heterojunction solar cells. Phys. Rev. B *82*, 245207. https://doi.org/10.1103/PhysRevB.82.245207.
68. Koopmans, M., Corre, V., and Koster, L. (2022). SIMsalabim: An open-source drift-diffusion simulator for semiconductor devices. J. Open Source Softw. *7*, 3727. https://doi.org/10.21105/joss.03727.
69. (2023). Bayesian Optimization for Automated Research. https://i-meet.github.io/boar/.
70. Jain, A., Kumar, P., Jain, S.C., Kumar, V., Kaur, R., and Mehra, R.M. (2007). Trap filled limit voltage (V_{TFL}) and V^2 law in space charge limited currents. J. Appl. Phys. *102*, 094505. https://doi.org/10.1063/1.2802553.
71. Le Corre, V.M., Duijnstee, E.A., El Tambouli, O., Ball, J.M., Snaith, H.J., Lim, J., and Koster, L.J.A. (2021). Revealing Charge Carrier Mobility and Defect Densities in Metal Halide Perovskites via Space-Charge-Limited Current Measurements. ACS Energy Lett. *6*, 1087–1094. https://doi.org/10.1021/acsenergylett.0c02599.
72. Zhou, H., Zhang, Y., Seifter, J., Collins, S.D., Luo, C., Bazan, G.C., Nguyen, T.Q., and Heeger, A.J. (2013). High-efficiency polymer solar cells enhanced by solvent treatment. Adv. Mater. *25*, 1646–1652. https://doi.org/10.1002/adma.201204306.
73. Leong, W.L., Cowan, S.R., and Heeger, A.J. (2011). Differential resistance analysis of charge carrier losses in organic bulk heterojunction solar cells: Observing the transition from bimolecular to trap-assisted recombination and quantifying the order of recombination. Adv. Energy Mater. *1*, 517–522. https://doi.org/10.1002/aenm.201100196.
74. Chen, Y., Wang, S., Xue, L., Zhang, Z., Li, H., Wu, L., Wang, Y., Li, F., Zhang, F., and Li, Y. (2016). Insights into the working mechanism of cathode interlayers in polymer solar cells via $[(C_8H_{17})_4N]_4[SiW_{12}O_{40}]$. J. Mater. Chem. A *4*, 19189–19196. https://doi.org/10.1039/C6TA08268H.
75. Khenkin, M.V., Katz, E.A., Abate, A., Bardizza, G., Berry, J.J., Brabec, C., Brunetti, F., Bulović, V., Burlingame, Q., Di Carlo, A., et al. (2020). Consensus statement for stability assessment and reporting for perovskite photovoltaics based on ISOS procedures. Nat. Energy *5*, 35–49. https://doi.org/10.1038/s41560-019-0529-5.
76. Heumueller, T., Mateker, W.R., Sachs-Quintana, I.T., Vandewal, K., Bartelt, J.A., Burke, T.M., Ameri, T., Brabec, C.J., and McGehee, M.D. (2014). Reducing burn-in voltage loss in polymer solar cells by increasing the polymer crystallinity. Energy Environ. Sci. *7*, 2974–2980. https://doi.org/10.1039/C4EE01842G.
77. Wang, Z., Wang, H., Yang, L., Du, M., Gao, L., Guo, Q., and Zhou, E. (2024). Selenophene-fused Perylene Diimide-Based Cathode Interlayer Enables 19 % Efficiency Binary Organic Solar Cells via Stimulative Charge Extraction. Angew. Chem. Int. Ed. Engl. *63*, e202404921. https://doi.org/10.1002/anie.202404921.
78. Saladina, M., Wöpke, C., Göhler, C., Ramirez, I., Gerdes, O., Liu, C., Li, N., Heumüller, T., Brabec, C.J., Walzer, K., et al. (2023). Power-Law Density of States in Organic Solar Cells Revealed by the Open-Circuit Voltage Dependence of the Ideality Factor. Phys. Rev. Lett. *130*, 236403. https://doi.org/10.1103/PhysRevLett.130.236403.
79. Mazzolini, E., Qiao, Z., Muller, J., Furlan, F., Sanviti, M., Nodari, D., Rimmele, M., Collauto, A., Deibel, C., Heeney, M., et al. (2025). Discerning Blend Microstructure and Charge Recombination for Stable Bio-renewable-Based Organic Photovoltaics. Adv. Energy Mater. 2405635. https://doi.org/10.1002/aenm.202405635.
80. Yuan, J., Zhang, Y., Zhou, L., Zhang, G., Yip, H.L., Lau, T.K., Lu, X., Zhu, C., Peng, H., Johnson, P.A., et al. (2019). Single-Junction Organic Solar Cell with over 15% Efficiency Using Fused-Ring Acceptor with Electron-Deficient Core. Joule *3*, 1140–1151. https://doi.org/10.1016/j.joule.2019.01.004.
81. Lin, Y., He, Q., Zhao, F., Huo, L., Mai, J., Lu, X., Su, C.J., Li, T., Wang, J., Zhu, J., et al. (2016). A Facile Planar Fused-Ring Electron Acceptor for As-Cast Polymer Solar Cells with 8.71% Efficiency. J. Am. Chem. Soc. *138*, 2973–2976. https://doi.org/10.1021/jacs.6b00853.
82. Zhu, L., Zhang, M., Xu, J., Li, C., Yan, J., Zhou, G., Zhong, W., Hao, T., Song, J., Xue, X., et al. (2022). Single-junction organic solar cells with over 19% efficiency enabled by a refined double-fibril network morphology. Nat. Mater. *21*, 656–663. https://doi.org/10.1038/s41563-022-01244-y.